CrossMark

Influence of inclusion type on the very high cycle fatigue properties of 18Ni maraging steel

Ulrike Karr[1], Reinhard Schuller[1], Michael Fitzka[1], Bernd Schönbauer[1], Duc Tran[2], Bert Pennings[2], and Herwig Mayer[1,*]

[1] Institute of Physics and Materials Science, BOKU, Peter-Jordan-Str. 82, 1190 Vienna, Austria
[2] Advanced Engineering, Bosch Transmission Technology, Dr. Hub van Doorneweg 120, P.O. Box 500, 5000 AM Tilburg, The Netherlands

ABSTRACT

The very high cycle fatigue (VHCF) properties of four 18Ni maraging steels were investigated. Ultrasonic fatigue tests were performed on thin sheets with nitrided surfaces at load ratio $R = 0.1$. Traditional maraging steel containing Ti (material A) showed crack initiation at TiN-inclusions. The elimination of Ti and the increase in Co content (material B) lead to preferential crack initiation at aluminate-inclusions. Aluminate-inclusions are less damaging than TiN-inclusions, and material B shows higher VHCF strength than material A. A further developed maraging steel (material C) with reduced Co content that is compensated for by alloying with Al showed crack initiation at aluminate- as well as at Zr(N,C)-inclusions. Zr(N,C)-inclusions are more damaging than aluminate-inclusions and less damaging than TiN-inclusions. The highest VHCF strength was found for a recently developed alloy with further increased Al content (material D). In addition to inclusion-initiated fracture, this material showed shear mode crack initiation in the nitrided zone at the surface.

Introduction

Maraging steels show an exceptional combination of very high mechanical strength and excellent manufacturing properties. Cooling to room temperature after solution annealing or austenitising treatment yields a relatively soft and very tough martensite due to the very low carbon content. Advantages for the fabrication of components are good formability and machinability in martensitic condition, low strain hardening during cold working, as well as excellent weldability. Practically, no dimensional changes and no cracking are associated with the subsequent hardening treatment. Precipitation hardening at moderate temperatures leads to the formation of intermetallic compounds that are responsible for the very high strength. Nitriding treatment can be applied for surface hardening due to the good nitridability. These excellent functional properties make maraging steels a potentially attractive material for highly stressed components.

Cyclic loads are present in several of the actual applications of maraging steels, such as springs or

Address correspondence to E-mail: herwig.mayer@boku.ac.at

components of the drive train in vehicles. The numbers of load cycles in these applications can be very high which explains the interest in the very high cycle fatigue (VHCF) properties of these materials. Ishii et al. [1] performed ultrasonic fatigue tests at load ratio $R = -1$ with four 18Ni maraging steels with about 1870 MPa tensile strength containing inclusions of different sizes. A transition of crack initiation from the surface to the interior at Ti(N,C)-inclusions was observed when the number of cycles to failure increased beyond 10^7. Mean lifetimes in the regime of 10^9 cycles were found at stress amplitudes between 300 and 400 MPa, where the materials with smaller inclusions showed higher cyclic strengths. Wang et al. [2] tested maraging steel with a tensile strength of 2800 MPa at load ratio $R = 0.1$. They observed a change from surface crack initiation to preferential initiation at interior inclusions as lifetimes increased beyond 10^6 cycles. A mean lifetime of about 10^7 cycles was found at a stress amplitude of 470 MPa. The relatively low cyclic strength in relation to the very high static strength was attributed to cyclic softening and growth of precipitates during cyclic deformation. Moriyama et al. [3] and Kawagoishi et al. [4] studied the influence of shot peening on the fatigue strength of 18Ni maraging steel. Rotating bending fatigue tests showed that the S–N curve measured with shot-peened specimens was shifted towards higher stress amplitudes compared with the untreated material due to the beneficial influence of surface compression stresses. Surface crack initiation in the HCF regime and interior crack initiation at inclusions in the VHCF regime was observed for the shot-peened material [3, 4].

Nitriding is an effective method to increase the wear resistance and can also have beneficial influences on the fatigue strength. The high surface hardness and compressive residual stresses in the nitrided surface layer increased the measured cyclic strength, in particular in rotating bending [5–7] and reversed bending experiments [8], where a stress gradient results in maximum cyclic stresses at the surface. Compressive residual stresses superimpose to the applied load and thus reduce the mean stress at the surface. This drives crack initiation towards the interior where the stress amplitude is reduced, and consequently, the fatigue strength is increased [5–7]. These beneficial influences were especially pronounced in the HCF regime, where unnitrided material showed surface crack initiation, while

nitrided material featured internal crack initiation [7]. In the VHCF regime, where internal crack initiation occurs for both surface conditions, the effect of nitriding, however, was found to be small [7]. Under cyclic axial loading conditions, beneficial effects of nitriding were found at high stress amplitudes, where cracks in the unnitrided and the nitrided material initiated at the surface and in the interior, respectively, whereas the influences diminished in the long lifetime regime with internal crack initiation for both surface conditions [9].

The effect of nitriding on the cyclic strength of 18Ni maraging steel was studied by Wang et al. [10]. Rotating bending experiments showed a distinct increase in cyclic strength in the shorter lifetime regime as fatigue crack initiation was shifted from the surface in the unnitrided material towards the interior in the presence of a nitrided surface layer. Hussain et al. [11] reported prolonged lifetimes of 18Ni nitrided maraging steel in cyclic bending experiments for stress amplitudes where cracks initiated at the subsurface in the nitrided and at the surface in the unnitrided material. HCF and VHCF properties of three nitrided 18Ni maraging steels have been studied in previous investigations in the authors laboratory [12, 13]. Fatigue cracks started exclusively in the interior at inclusions whose sizes affected fatigue lifetime and cyclic strength. No fatigue limit was observed below 10^9 cycles.

Some findings on the VHCF properties of maraging steels may be well expected on the basis of the VHCF literature. S–N curves of high-strength steels often do not show a fatigue limit. Fatigue cracks starting at internal non-metallic inclusions are a main reason for failures in the VHCF regime [14–16]. However, cracks can also start in the interior without the presence of inclusions [17, 18] or at the surface [19–21]. A survey of experimental data and models of inclusion-induced VHCF failures in high-strength steels can be found in [22]. Crack initiating mechanisms and early crack growth for virtually defect-free materials are reviewed in [23]. Ultrasonic fatigue testing is often used for VHCF studies, and a review of new applications and recent experimental results obtained with this technique is published in [24].

Most studies of the VHCF properties are performed under cyclic tension–compression conditions. Preloading can have pronounced influences on crack initiation and early crack growth. Some steels show VHCF failures only at positive load ratios and not

under fully reversed loading conditions [25, 26]. It was demonstrated that optically dark areas (ODAs) [27, 28] which are a typical feature on the fracture surface in the vicinity of internal inclusions are solely formed at negative but not at positive load ratios [26]. The influence of inclusions, that cause crack initiation in the VHCF regime, is mainly determined by the size of the inclusion, i.e. the larger the inclusion, the shorter the fatigue lifetime and the lower the cyclic strength. Additionally, the hardness of the matrix material affects the cyclic strength in the presence of inclusions [29, 30]. Equations used to predict the VHCF strength typically consider the projected area of the inclusion and the Vickers hardness of the matrix [31]. More recent investigations show, however, that also the type of inclusion is important for the harmful influence of inclusions on VHCF strength [32, 33].

In the present work, the cyclic properties of four maraging steels with different chemical compositions are studied. Thin sheets with nitrided surfaces are tested in the HCF and VHCF regime at load ratio $R = 0.1$ with ultrasonic fatigue testing equipment. The high cycling frequency in the range of 20 kHz allows measurements extending into the VHCF regime within reasonable testing times. Experiments are performed on a traditional Ti-containing maraging steel (material A), a Ti-free maraging steel (material B) and two newly developed maraging steels with reduced Co and increased Al and Cr content (materials C and D). Comparable materials are actually used (materials A and B) for push belts in continuously variable transmission (CVT). The newly developed materials (materials C and D) are candidates for this application where high cyclic strength in the VHCF regime is a most important requirement. The present investigation is therefore of great practical interest for maraging steels that are used in the very long lifetime regime.

Material and method

Material

Fatigue tests are performed on four 18Ni maraging steels in precipitation-hardened condition. Thin sheets with nitrided surfaces are tested. The respective chemical compositions of the four materials are

Table 1 Chemical composition of the four investigated maraging steels in weight%

	Ni	Co	Mo	Ti	Al	Cr	Fe
Material A	18	9	5	0.5	–	–	Balance
Material B	18	16.5	5	–	–	–	Balance
Material C	18	5	5	–	1	1	Balance
Material D	18	5	5	–	1.5	1	Balance

shown in Table 1. The materials are characterised as follows:

- Material A: This material is a traditional Ti-containing maraging steel. Hardening leads to the formation of Ni_3Ti, Ni_3Mo and Fe_2Mo intermetallic compounds that strengthen the material [34].

- Material B: The chemical composition shows no Ti and a higher Co content than material A. Ti is eliminated in material B to avoid TiN-type non-metallic inclusions that were found to act as sources for fatigue cracks. Co increases the strength since it lowers the solubility of Mo and increases the amount of Ni_3Mo and Fe_2Mo during hardening [34].

- Material C: The Co content is lower than in materials A and B for economic rather than technical reasons. The reduced Co content is compensated for by an increased amount of Al and Cr. Aluminium exhibits limited solubility in the iron-nickel martensite, which promotes the formation of intermetallic precipitates such as NiAl and Ni_3Al and increases the hardness [35]. Cr is beneficial for nitriding since it forms very small CrN precipitates in the diffusion zone that strengthen the material at the surface.

- Material D: This material is comparable to material C, but with further increased aluminium content.

Precipitation hardening of all four materials was performed at 480 °C for about 2–3 h. After the maraging heat treatment, specimens were gas nitrided for one hour at a temperature below 480 °C. In order to measure the depth of the nitrogen diffusion zone, microsections were made from the specimens which were subsequently etched to reveal the diffusion zone. Additionally, the nitrogen diffusion depth was measured by glow discharge optical emission spectroscopy. The depth of the diffusion zone is in

the range of 30 ± 3 µm for all four materials. After the hardening and nitriding treatment, all materials exhibit a precipitation-hardened martensitic microstructure.

The Vickers hardness beneath the nitrided surface layer was determined by making microsections from the specimens and indenting in the centre of the cross section with an indention force of 1 kp. Two indentions were evaluated on four samples of each material. Vickers hardness obtained with eight measurements is 580 $HV_{1.0}$ for material A, 625 $HV_{1.0}$ for material B, 560 $HV_{1.0}$ for material C and 615 $HV_{1.0}$ for material D.

The Vickers hardness of the nitrided layer was measured directly at the outer surface of the fatigue specimens without making microsections. An indention force of 0.1 kp was used. Four samples for each material with five measurements per sample revealed a surface hardness of 1000 ± 50 $HV_{0.1}$ for all four materials.

Tensile strength could not be measured using fatigue specimens directly. However, based on measurements of components made of these materials a reasonable estimate is 1800 MPa for the yield strength and 2000 MPa for the tensile strength for all four materials.

The shape of the specimens used in the present investigation is shown in Fig. 1. The load bearing cross section is minimum in the centre of the specimen. Consequently, the stresses are maximum in the centre and decrease towards the ends of the specimens due to the increasing load bearing cross section. Maximum stresses in the centre are named nominal stresses. A volume of 4.1 mm^3 and a surface area of 27 mm^2, respectively, are subjected to greater than 90% of the nominal stress in materials A, B and D. For material C, the respective values are 5.1 mm^3 and 34 mm^2. The volume and the surface area subjected to greater than 95% of the nominal stress are 2.7 mm^3 and 18 mm^2, respectively, for materials A, B and D. For material C, the values are 3.4 mm^3 and 22 mm^2, respectively. The edges in the centre regime of the sheets are rounded off (radius between 0.09 and 0.10 mm).

Fatigue cracks are initiated in the middle section of the specimens, however, not necessarily exactly in the centre. Therefore, stresses at the site of crack initiation can be somewhat lower than the nominal stress in the centre. The location of the crack initiation site is determined for each failed specimen, and the actual stress is calculated. For the presentation of fatigue data in the S–N diagrams as well as for all other evaluations, the actual stress at the crack initiation site is used. Cyclic and static stresses vary in equal measure relative to the cross section, and the load ratio of R = 0.1 used in the present study is the same for all crack initiation sites. Data of runout specimens are presented using the nominal stresses.

Method

The experiments were performed using ultrasonic fatigue testing equipment developed at BOKU University [24]. The method to test thin sheets of high-strength steels has been described in detail in previous works [12, 13]. In brief, rather than vibrating in resonance, the sheet specimens (Fig. 1) are screw-mounted onto a dumbbell-shaped carrier specimen. The thin sheet specimens are pre-stressed and driven to joint vibration with the carrier specimen. The carrier specimen serves to introduce the static and cyclic loads into the thin sheet specimens and additionally serves to avoid buckling and undesirable bending vibrations.

At the lower end of the carrier specimen, the load train is extended by a rod of two wavelengths length. This serves to introduce static stresses into the sheet specimens and enables tests at load ratio R = 0.1. To apply static loads, the carrier specimen is bent and the thin sheet specimen is mounted. Subsequently, carrier specimen and rod are released and readjusted to vertical alignment by a balancing weight. The magnitude of the hereby applied pre-stress is verified by means of two strain gages attached to front and
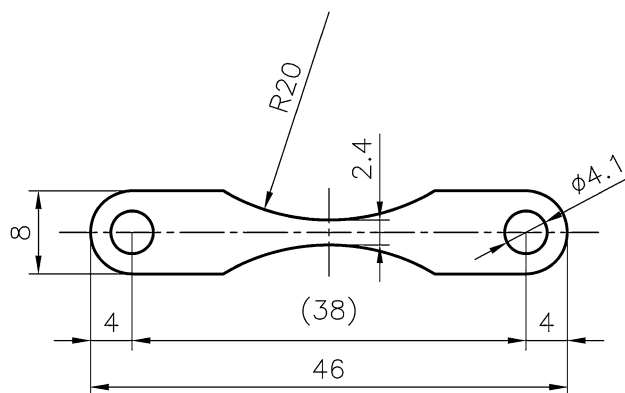

Figure 1 Sheet specimens used in the ultrasonic fatigue tests (all measures in mm). Thickness of specimens is 0.35 mm for materials A, B and D and 0.435 mm for material C.

back side of the thin sheet specimens. Thereby, it is guaranteed that the static stresses at both sides of the specimen are equal.

The strain gauges are also used to calibrate the cyclic stresses. The measured strain amplitude of the sheet specimens and the vibration amplitude of the carrier specimen are proportional. The vibration amplitude serves to control the magnitude of cyclic loading in a closed-loop circuit and is measured with a vibration gauge. The load is applied in a pulsed mode (pulse length is typically 100 ms, i.e. 2000 load cycles). Periodic pauses (pause length between 100 and 1000 ms) and forced air cooling serve to avoid heating of the specimen. The temperatures at the surface of the specimens are monitored with an

infrared thermometer. Experiments are performed in a climatised laboratory in ambient air at 20 °C and 50% relative humidity. Fractographic investigations are conducted using a scanning electron microscope (SEM). Crack initiating inclusions were analysed using energy-dispersive X-ray spectroscopy (EDS).

Results

Fatigue properties in the HCF and VHCF regime of four 18Ni maraging steels have been investigated at load ratio $R = 0.1$. S–N data of nitrided thin sheet specimens are shown in Fig. 2. Different symbols are used to denote the different crack initiation sites, i.e.
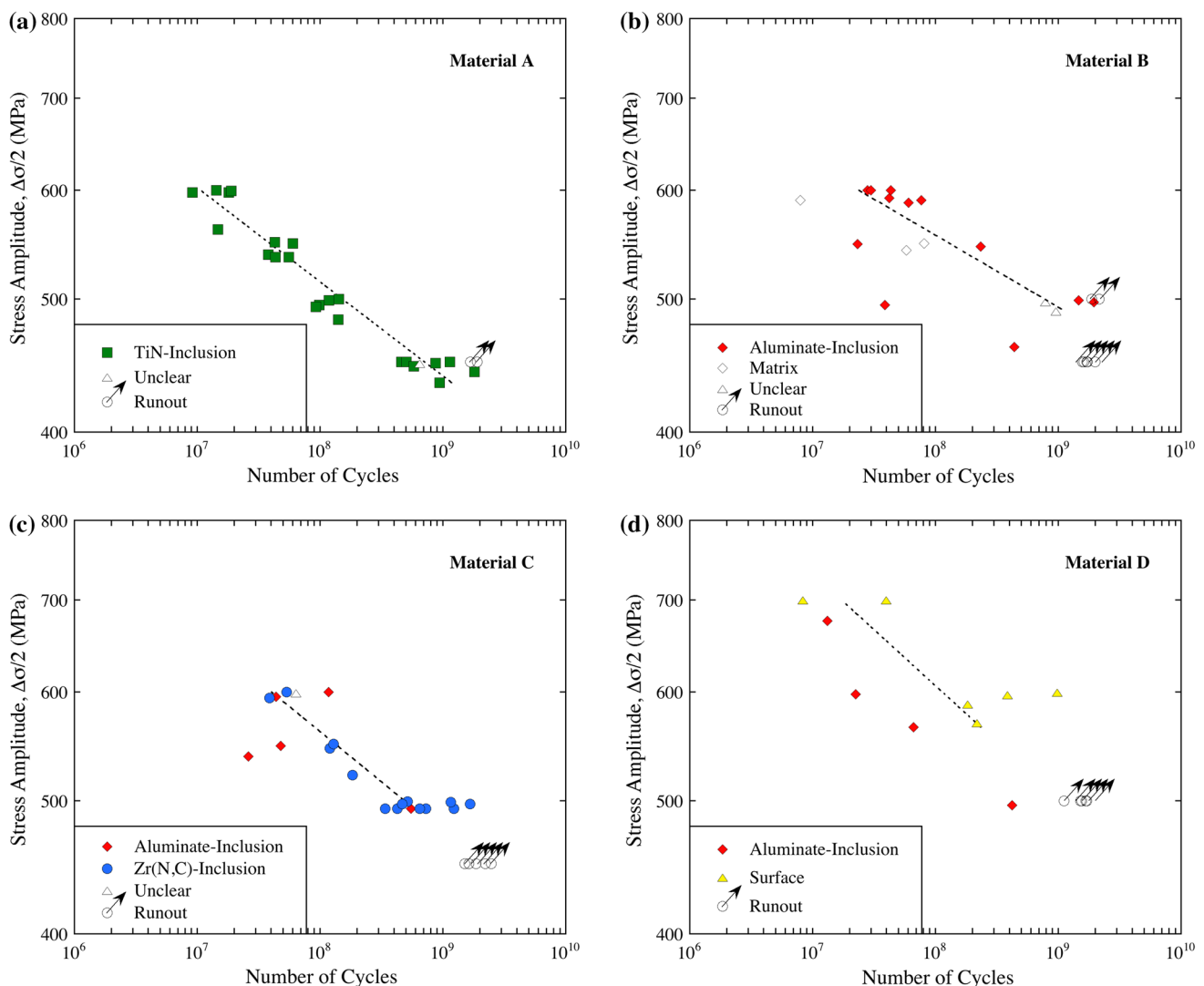

Figure 2 S-N data of nitrided 18Ni maraging steel sheets measured at load ratio $R = 0.1$ **a** for material A, **b** for material B, **c** for material C and **d** for material D, respectively. Different symbols are used to mark the different crack initiation locations.

at internal TiN-inclusions (green squares), internal aluminate-inclusions (red diamonds), internally in the matrix without the presence of an inclusion (open diamonds), internal Zr(N,C)-inclusions (blue circles) or at the surface (yellow triangles). Open triangles are used when the crack initiation could not be identified (e.g. due to a deformed fracture surface). Runouts are denoted with open circles and arrows. Data of fractured specimens are presented versus the respective actual stress amplitude at the crack initiation site. The nominal stress amplitude is used to characterise loading of runout specimens. S–N data are approximated with a straight line assuming a power law dependence between stress amplitudes, $\Delta\sigma/2$ (in MPa), and cycles to failure, N, similar to a Basquin equation:

$$N = C_B \cdot \left(\frac{\Delta\sigma}{2}\right)^{-n_B} \tag{1}$$

where C_B and n_B are material constants. Solely stress amplitudes with more than 50% failures are considered to determine the approximation lines. Assuming a log-normal distribution of fatigue lifetimes, the approximation lines represent 50% fracture probability [36]. Exponents n_B and constants C_B used to approximate data of the four materials are shown in Table 2.

S–N data of material A are shown in Fig. 2a. Internal crack initiation at TiN-inclusions is found in 22 of 23 fractured specimens. In one specimen, the crack initiation site is unclear. Stress amplitudes between 600 and 434 MPa correspond to lifetimes between 9.1×10^6 and 1.8×10^9 cycles. Two specimens did not fail during the experiments. No endurance limit was observed within the investigated regime.

S–N data measured with material B are shown in Fig. 2b. Crack initiation at internal aluminate-inclusions is found in 12 of 17 fractured specimens. In three specimens, the crack was initiated internally in

the matrix, and in two specimens, the crack initiation site is unclear.

S–N data of material C are shown in Fig. 2c. Of 20 fractured specimens, cracks are initiated at an internal aluminate- and an internal Zr(N,C)-inclusion in 5 and 14 specimens, respectively. In one specimen, the crack initiation is unclear.

S–N data of material D are shown in Fig. 2d. In 4 specimens, the crack started at an internal aluminate-inclusion. Six specimens failed with the fatigue crack initiating at the surface. Surface crack initiation was exclusively found for material D. Specimens showing surface failure tend to fail at higher numbers of cycles than specimens with internal inclusion-initiated failures.

The stress amplitude leading to a mean lifetime of 10^8 cycles may be used to compare the cyclic strengths of the four materials in the VHCF regime. This stress amplitude is 510 MPa for material A and 560 MPa for material B and C, respectively. Material D shows the highest cyclic strength with 610 MPa.

Fracture surfaces of the four materials are shown in Figs. 3, 4, 5 and 6. Figure 3a shows an overview of the fracture surface of a specimen of material A. A fish-eye with an elongated shape is visible at the source of the crack. The crack initiation site is shown in more detail in Fig. 3b revealing a fractured inclusion. No cracking of the boundary between inclusion and matrix is visible, indicating fracture of the inclusion rather than interface fracture. The EDS analysis of the inclusion shown in Fig. 3c suggests a TiN non-metallic inclusion. Comparable EDS results were obtained for all crack initiating inclusions in material A. The fracture surface shows a fine and granular appearance adjacent to the inclusion. As the crack length reaches 25–40 µm, the crack path deflects from its initial propagation direction perpendicular to the maximum tensile stress. The crack continues to grow in shear mode, while the fracture morphology appears rather smooth and somewhat smeared exhibiting shallow, elongated dimples.

An overview of the fracture surface of a specimen of material B is shown in Fig. 4a, revealing a fish-eye with an approximately equiaxed shape and an inclusion. The inclusion is shown at higher magnification in Fig. 4b. The fracture surface close to the inclusion appears fine and granular. The inclusion is uncracked, while apparently the interface between inclusion and matrix has failed. From the EDS analysis shown in Fig. 4c, it is concluded that the crack

Table 2 Exponents n_B and constants C_B used to approximate data in Fig. 2 according to Eq. (1); stress amplitudes, $\frac{\Delta\sigma}{2}$, are in MPa

	N_B	C_B
Material A	14.61	4.09×10^{47}
Material B	19.09	2.59×10^{60}
Material C	13.68	3.98×10^{45}
Material D	12.27	1.38×10^{42}

Figure 3 Fatigue crack initiation at an internal TiN-inclusion in material A; $\Delta\sigma/2 = 539$ MPa, $N = 3.8 \times 10^7$ cycles; **a** fracture surface; **b** detail of the crack initiating inclusion; **c** EDS analysis of the crack initiating inclusion.
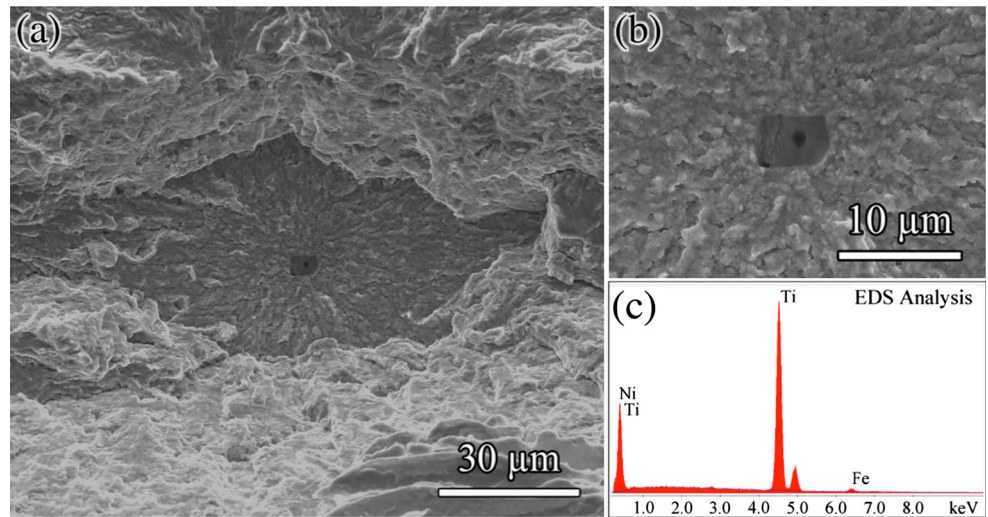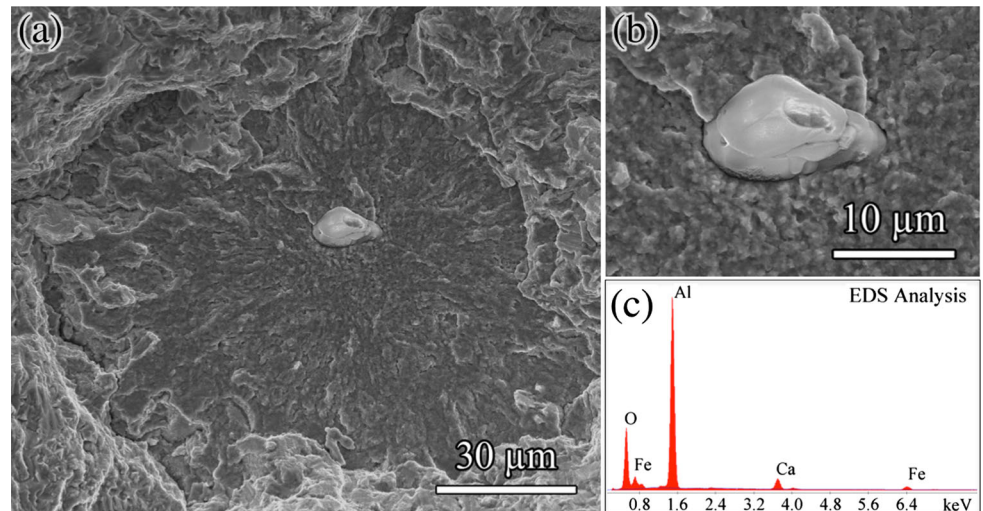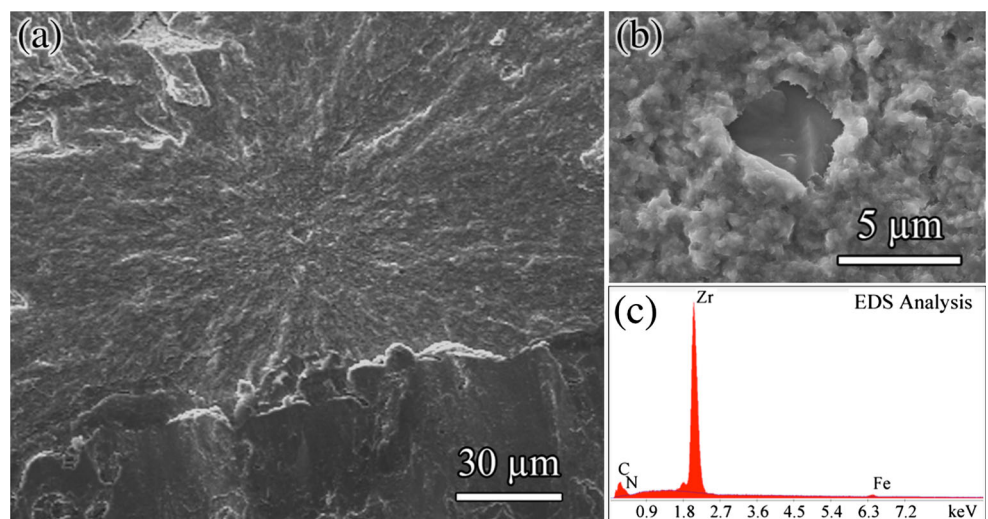

Figure 4 Fatigue crack initiation at an internal aluminate-inclusion in material B; $\Delta\sigma/2 = 495$ MPa, $N = 3.9 \times 10^7$ cycles; **a** fracture surface; **b** detail of the crack initiating inclusion; **c** EDS analysis of the crack initiating inclusion.

Figure 5 Fatigue crack initiation at an internal Zr(N,C)-inclusion in material C; $\Delta\sigma/2 = 497$ MPa, $N = 1.7 \times 10^9$ cycles; **a** fracture surface; **b** detail of the crack initiating inclusion; **c** EDS analysis of the crack initiating inclusion.
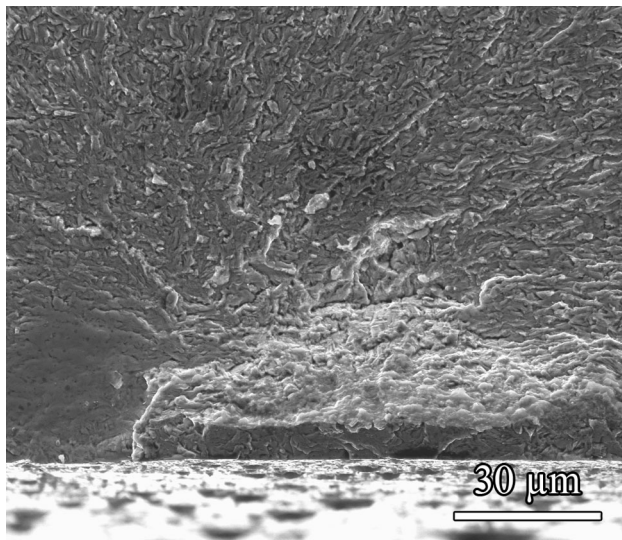
Figure 6 Fatigue crack initiation at the surface in material D; $\Delta\sigma/2 = 588$ MPa, $N = 1.8 \times 10^8$ cycles.

Figure 7 Fatigue lifetimes measured for specimens with crack initiation at TiN-inclusions (in material A), at Zr(N,C)-inclusions (in material C), at aluminate-inclusions (in material B (*filled red diamond*), material C (*top filled red diamond*) and material D (*bottom filled red diamond*), and at the surface (in material D), respectively.

started at an aluminate-inclusion. All crack initiating particles in material B are aluminate-inclusions. Similar to material A, the crack initially propagates perpendicular to the maximum tensile stress and changes to shear mode as the crack length reaches 40–50 μm. Secondary cracks are visible in the transition zone.

The fracture surface of a specimen of material C that failed after more than 10^9 cycles is shown in Fig. 5a. Figure 5b shows the crack initiating inclusion in more detail. The inclusion is fractured, i.e. the initial crack is formed due to failure of the inclusion rather than the interface. EDS analysis of the internal inclusion shown in Fig. 5c suggests that the particle is a Zr(N,C)-inclusion. In 14 specimens of material C, the crack was initiated at an Zr(N,C)-inclusion. Aluminate-inclusions were found at the crack initiation location of five specimens of material C. The fracture surface within a radius of about 15 μm around the inclusion features a fine and granular appearance. No distinct change of crack growth from tensile to shear mode is found in this material.

Figure 6 shows the fracture surface of a specimen of material D featuring crack initiation at the surface. The initial crack propagates perpendicular to the maximum tensile stress for the first 4 μm; then, the crack path changes to shear mode. At approximately 30 μm, the crack deflects again and grows perpendicular to the loading direction until final failure. The depth of about 30 μm corresponds to the transition
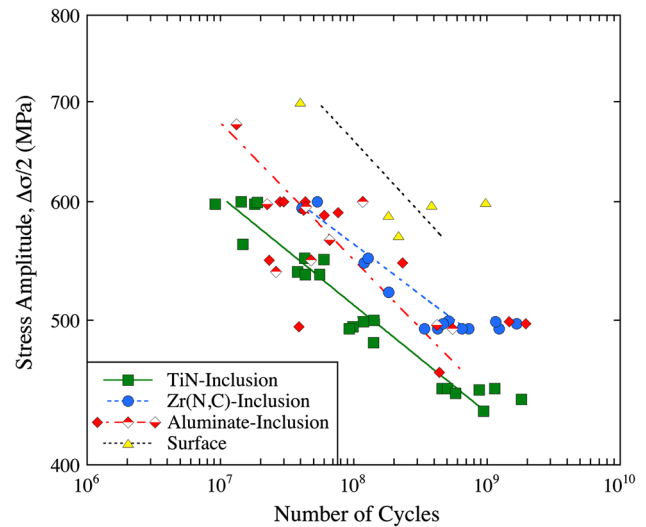
between the hard nitrided surface layer and the softer matrix.

Figure 7 presents the numbers of cycles to failure distinguishing the four identified types of crack initiation sites. Specimens with surface crack initiation show the highest cyclic strength. On average, the lowest cyclic strength is found for specimens with crack initiation at TiN-inclusions. Specimens with crack initiation at Zr(N,C)-inclusions exhibit the longest lifetimes of all specimens with interior inclusion-initiated fracture. The largest scatter of lifetimes is found for specimens with crack initiation at aluminate-inclusions. Here, some specimens fail earlier than specimens with TiN-inclusions and others live longer than specimens with Zr(N,C)-inclusions.

The size of an inclusion is most important to characterise its harmful influence on the VHCF strength. Therefore, the sizes of the crack initiating inclusions were determined. The projected areas of the inclusions perpendicular to the specimens' length axes, i.e. in the direction of maximum principal stress, $area_{INC}$, are determined by evaluating SEM images. The sizes of inclusions are quantified by the square root of their projected areas, $\sqrt{area_{INC}}$. The sizes of crack initiating TiN-inclusions are in the range from 2.5 to 5.3 μm for material A. Material B

contains crack initiating aluminate-inclusions with $3.7\ \mu m \le \sqrt{area_{INC}} \le 9.6\ \mu m$. Material C shows crack initiation at Zr(N,C)-inclusions and aluminate-inclusions in the range of $2.2\ \mu m \le \sqrt{area_{INC}} \le 4.4\ \mu m$ and $4.5\ \mu m \le \sqrt{area_{INC}} \le 7.9\ \mu m$, respectively. The sizes of crack initiating aluminate-inclusions in material D range from 4.9 to 9.5 μm.

Discussion

Inclusions are the main source of fatigue cracks in materials A, B and C. The crack started at internal inclusions in 96% of the failed specimens of material A, in 71% of the failures of material B and in 95% of the failures of material C. Solely, material D shows crack initiation at the surface in 60% of the failed specimens and internal inclusions in 40% of the failed specimens. However, the earliest failures in material D are caused by internal inclusions. These results indicate a prominent influence of internal inclusions on the fatigue damage mechanism, the cyclic strength and the fatigue lifetime of the investigated maraging steels. The nitrided surface zone favours crack initiation in the interior due to its high hardness and compressive residual stresses [5–7]. Additionally, high-strength steels generally tend to fracture from interior inclusions rather than from the surface when lifetimes are in the VHCF regime.

Fatigue lifetimes and cyclic strengths decrease with increasing size of the crack initiating inclusions. Murakami and Endo [29, 30] showed that in the presence of a small cavity or a secondary phase particle, the endurance limit, σ_W, can be correlated with the square root of the projected area of the inhomogeneity, $\sqrt{area}$, as shown in Eq. (2).

$$\sigma_w^6 \cdot \sqrt{area} = C_M \qquad (2)$$

The parameter C_M considers the position of the inhomogeneity (at the surface or in the interior), the Vickers hardness of the material and the load ratio [37].

Equation (2) suggests that the cyclic stress amplitude, $\Delta\sigma/2$, and the square root of the inclusion area, $\sqrt{area_{INC}}$, can be combined to the parameter $\frac{\Delta\sigma}{2} \cdot \left(\sqrt{area_{INC}}\right)^{\frac{1}{6}}$ that characterises the damage of a fatigue load cycle in the presence of an inclusion. The number of cycles to failure, N, can be presented versus this parameter according to Eq. (3) [20].
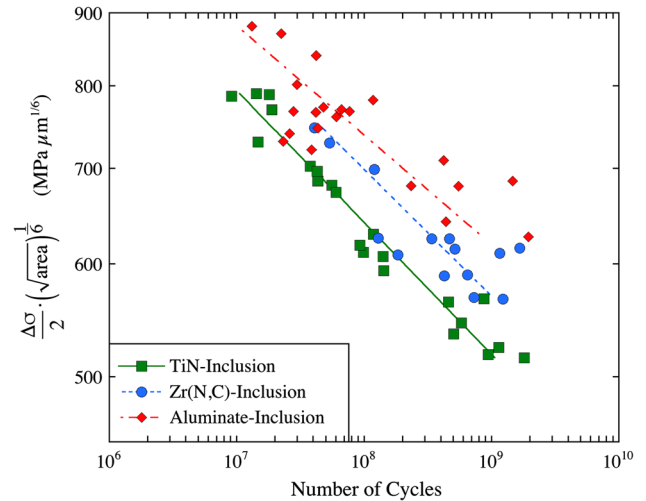

Figure 8 Cycles to failure of specimens with inclusion-initiated failures presented as a function of the parameter $\frac{\Delta\sigma}{2} \cdot \left(\sqrt{area_{INC}}\right)^{\frac{1}{6}}$.

$$N = C_A \cdot \left(\frac{\Delta\sigma}{2} \cdot \left(\sqrt{area_{INC}}\right)^{\frac{1}{6}}\right)^{-n_A} \qquad (3)$$

where C_A and n_A are material constants.

Figure 8 shows the fatigue lifetimes on the abscissa as a function of $\frac{\Delta\sigma}{2} \cdot \left(\sqrt{area_{INC}}\right)^{\frac{1}{6}}$ on the ordinate for the different inclusion types, with stress amplitudes in MPa and $\sqrt{area_{INC}}$ in μm. Linear lines in the double-logarithmic plots show the approximation of the data assuming a power law dependence according to Eq. (3). Exponents n_A and constants C_A used to approximate data of the three inclusion types are shown in Table 3. The approximation lines indicate different damaging influences of the three inclusion types: TiN-inclusions are the most and aluminate-inclusions the least damaging among the three. It must be mentioned that this is no effect of inclusion size, which is already considered in the parameter $\frac{\Delta\sigma}{2} \cdot \left(\sqrt{area_{INC}}\right)^{\frac{1}{6}}$, but an effect of inclusion type.

However, Fig. 8 demonstrates the influence of inclusion size and type on the measured lifetimes

Table 3 Exponents n_A and constants C_A used to approximate data in Fig. 8 according to Eq. (3); stress amplitudes, $\frac{\Delta\sigma}{2}$, are in MPa and $\sqrt{area_{INC}}$ in μm

	N_A	C_A
TiN-inclusions	10.80	2.07×10^{38}
Zr(N,C)-inclusions	11.25	1.00×10^{40}
Aluminate-inclusions	13.01	2.14×10^{45}

evaluating inclusions that are found in four different maraging steels. This raises the question about possible influences of the matrix material. Material C shows Zr(N,C)—as well as aluminate-inclusions but does not contain TiN-inclusions, and therefore, a direct comparison of all three inclusion types in the same matrix material is not possible. On the other hand, aluminate-inclusions were found in materials B, C and D, which allows to estimate possible influences of the matrix on the measured lifetimes for these steels. Sizes of aluminate-inclusions in the three materials are in a comparable range: $3.7\ \mu m \leq \sqrt{\text{area}_{\text{INC}}} \leq 9.6\ \mu m$ for material B, $4.5\ \mu m \leq \sqrt{\text{area}_{\text{INC}}} \leq 7.9\ \mu m$ for material C and $4.9\ \mu m \leq \sqrt{\text{area}_{\text{INC}}} \leq 9.5\ \mu m$ for material D. Experiments with comparable load levels have been performed with these materials. Figure 7 shows that for stress amplitudes between 490 and 500 MPa, the earliest as well as the latest failure was found for specimens made of material B. At stress amplitudes between 538 and 550 MPa, the earliest and the latest failures were found also for material B. In experiments with stress amplitudes between 588 and 600 MPa, the earliest failure is found for material D and the latest failure for material C. Specimens with aluminate-inclusions in materials B, C and D show failures in a comparable range of cycles and do not suggest a pronounced influence of the matrix material. Therefore, it seems reasonable to consider different cyclic strength in the presence of inclusions to be mainly caused by the inclusion size, the inclusion type and to a smaller extent by possible influences of the matrix material.

Another method to consider the influence of cyclic loads and sizes of crack initiating inclusions on fatigue lifetimes is based on a fracture mechanics concept, as suggested by Tanaka and Akiniwa [38]. The crack initiating inclusions are considered as initial cracks. It is assumed that fatigue lifetimes are equal to the number of cycles necessary to propagate the cracks to fracture. The underlying crack propagation law is an adapted Paris law, as shown in Eq. (4) [38, 39].

$$\frac{\Delta(\sqrt{\text{area}})}{\Delta N} = C_P \cdot \Delta K^{n_P} \tag{4}$$

where C_P and n_P are material constants. Crack propagation starts with the first cycle at initial growth rates, $\frac{\Delta(\sqrt{\text{area}})}{\Delta N}$, that are orders of magnitude below one atomic distance per cycle.

The stress intensity range, ΔK, of an arbitrarily shaped internal crack can be calculated as suggested by Murakami [40]:

$$\Delta K = 0.5 \cdot \Delta\sigma \cdot \sqrt{\pi \cdot \sqrt{\text{area}}} \tag{5}$$

Integrating the growth rates from the starting crack length $\sqrt{\text{area}_{INC}}$ to fracture delivers Eq. (6) [39].

$$\frac{N}{\sqrt{\text{area}_{\text{INC}}}} = \frac{2}{C_P(n_P - 2)} \cdot (\Delta K_{\text{INC}})^{-n_P} \tag{6}$$

With this method, the ratio of cycles to failure N and $\sqrt{\text{area}_{INC}}$ can be correlated with the stress intensity range ΔK_{INC}.

Figure 9 shows this correlation for the three different types of crack initiating inclusions. Data are approximated with straight lines in the double-logarithmic diagram assuming a power law dependence according to Eq. (6). Exponents n_P and constants C_P used to approximate data of the three inclusion types are shown in Table 4. The approximation line for
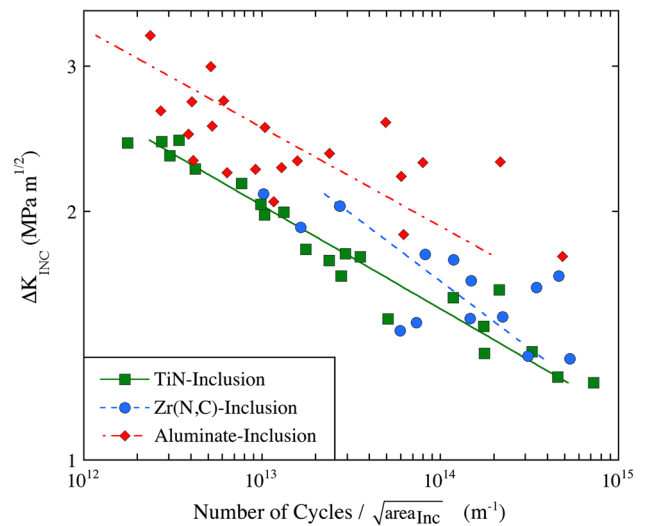

Figure 9 Ratio of cycles to failure and $\sqrt{\text{area}_{\text{INC}}}$ of specimens with inclusion-initiated failures presented as a function of the stress intensity range ΔK_{INC}.

Table 4 Exponents n_P and constants C_P used to approximate data in Fig. 9 according to Eq. (6); stress intensity ranges, ΔK_{INC}, are in MPam$^{1/2}$ and $\sqrt{\text{area}_{\text{INC}}}$ in m

	n_P	C_P
TiN-inclusions	7.80	1.18×10^{-16}
Zr(N,C)-inclusions	6.15	2.24×10^{-16}
Aluminate-inclusions	8.36	1.35×10^{-17}

data of TiN-inclusions lies at lower values of ΔK_{INC} than for aluminate-inclusions. The approximation line for data of Zr(N,C)-inclusions lies in between. The minimum stress intensity range, ΔK_{INC} leading to fracture, is 1.2 MPam$^{1/2}$ for TiN-inclusions, 1.3 MPam$^{1/2}$ for Zr(N,C)-inclusions and 1.8 MPam$^{1/2}$ for aluminate-inclusions. This confirms the result stated above: TiN-inclusions are more damaging than Zr(N,C)-inclusions, and Zr(N,C)-inclusions are more damaging than aluminate-inclusions.

Evaluating the detrimental influence of internal inclusions on the fatigue life of maraging steels, the difference in crack initiation between TiN- and Zr(N,C)-inclusions and aluminate-inclusions must be taken into account. TiN- and Zr(N,C)-inclusions (see Figs. 3, 5, respectively) are tightly bonded to the matrix and therefore fracture featuring a brittle fracture morphology. Smooth fracture surfaces and sharp crack tips are present after the inclusion failed, which facilitates the propagation of the initial crack into the matrix. In aluminate-inclusions, on the other hand, debonding of the interface between particle and matrix (see, for example, Fig. 4) results in an approximately spherical cavity. Stress concentration at the equator of a spherical cavity is about two, which favours crack initiation in that area. However, the crack first needs to be initiated at the border of the cavity after the interface failed in contrast to TiN- and Zr(N,C)-inclusions, where the fractured particle already acts as the initial crack. The additional load cycles required to initiate the crack at the cavity may explain the longer lifetimes observed for aluminate-inclusions compared to TiN- and Zr(N,C)-inclusions. This influence of crack initiation mechanism on VHCF properties is well in accordance with the literature. For high carbon–chromium steel SUJ2, Furuya et al. [32] found longer lifetimes and higher endurance limits for specimens featuring crack initiation at Al$_2$O$_3$-inclusions and interface fracture than for specimens with (Cr,Fe)C-inclusions where the fractured particles acted as crack starters. For the same high carbon–chromium steel, Spriestersbach et al. [33] found higher necessary stress intensity amplitudes to propagate a crack to fracture in the VHCF regime, when the crack started at a fractured interface between AlCaO- or CaO-inclusions and matrix than when it started at a fractured TiN-inclusion.

Comparing TiN- and Zr(N,C)-inclusions, the former are found to be more detrimental on fatigue lifetimes, which cannot be explained with a difference in crack initiation mechanism. Zr(N,C)-inclusions are found in material C and TiN-inclusions in material A. Possible differences in the matrix must be considered therefore. Hardness is considered an important material parameter that influences the cyclic properties in the VHCF regime in the presence of inclusions [29, 30]. Hardness of material A (580 HV) is slightly higher than of material C (560 HV) which is in contradiction to TiN-inclusions in material A being more harmful. Moreover, heat treatment of all investigated maraging steels is similar. This suggests that the different influence of TiN- and Zr(N,C)-inclusions on the VHCF strength may be attributed rather to the different inclusion type than to the matrix.

A possible explanation is based on the different thermal expansion coefficient of the two inclusion types and consequently different residual stresses after cooling. The thermal expansion coefficient, α_p, of Zr(N,C) is in the range of 7.6–7.8 × 10^{-6} K^{-1} [41] and 9.4 × 10^{-6} K^{-1} for TiN [42], whereas the thermal expansion coefficient of maraging steels, α_m, is about 10 × 10^{-6} K^{-1}. The relatively higher coefficient of thermal expansion of maraging steels leads to higher contraction during cooling of the material, inducing compressive residual stresses in the inclusion. Assuming a spherical shape of the inclusion Eq. (7) allows to calculate the compression stress p in the inclusion after cooling [43, 44].

$$p = \frac{(\alpha_m - \alpha_p) \cdot \Delta T}{\frac{1}{4G_m} + \frac{1}{3K_p}} \tag{7}$$

Shear modulus, G_m, of the matrix material (maraging steel) is 77 GPa. The bulk modulus, K_p, of the particle is 230 GPa for Zr(N,C)-inclusions and 280 GPa for TiN-inclusions [45]. Assuming stress-free conditions after the maraging and nitriding treatment at 480 °C, cooling to room temperature ($\Delta T = 460$ K) would lead to compressive residual stresses of 230 MPa in Zr(N,C)- and only 60 MPa in TiN-inclusions. It is assumed that under cyclic tension loading compressive residual stresses retard cracking of the inclusion and prolong the crack initiation period. The higher compressive residual stresses in Zr(N,C)-inclusions could therefore serve as explanation for possibly greater numbers of cycles required to crack this type of inclusions which consequently increases the fatigue lifetime.

Conclusion

Very high cycle fatigue (VHCF) properties of four nitrided 18Ni maraging steel sheets have been investigated at load ratio $R = 0.1$. The materials show similar static strength despite featuring different chemical compositions. Material A contains Ti, whereas the others do not. In material B, the lack of Ti is compensated for by an increase in Co content. The Co content is reduced in materials C and D and compensated for by addition of Al, with a higher amount of Al in material D than in material C.

The following results are found:

1. Material A shows the lowest and material D the highest VHCF strength, while materials B and C lie in between. The development of maraging steels from material A to D was successful in increasing the VHCF properties.
2. Fatigue crack initiation at internal inclusions is the most important crack initiating mechanism in the four materials although the sizes of the inclusions $\sqrt{\text{area}_{\text{INC}}}$ are very small (between 2 and 10 μm). Crack initiating particles are TiN-inclusions in material A and aluminate-inclusions in materials B and D. Material C shows aluminate- as well as Zr(N,C)-inclusions at the origins of the fatigue cracks. Only material D shows crack initiation in the nitrided surface layer as an additional crack initiating mechanism. Fatigue lifetimes and cyclic strength decrease with increasing size of the crack initiating inclusion for all inclusion types.
3. TiN-inclusions are found to be most, and aluminate-inclusions are found to be least damaging, while the detrimental influence of Zr(N,C)-inclusions on VHCF strength lies in between. Solely influences of inclusion size and type are considered. Possible influences of the matrix material are assumed to be small.
4. Considering the particles as initial cracks, VHCF failures occurred at minimum stress intensity ranges ΔK_{INC} of 1.2 MPam$^{1/2}$ for TiN-inclusions, 1.3 MPam$^{1/2}$ for Zr(N,C)-inclusions and 1.8 MPam$^{1/2}$ for aluminate-inclusions in tests at load ratio $R = -1$.
5. Interfacial fracture is found at aluminate-inclusions forming approximately spherical cavities which act as sources of fatigue cracks. Contrary, TiN- and Zr(N,C)-inclusions are tightly bonded to the matrix and do actually fracture, acting as the initial crack themselves. A relatively lower thermal expansion coefficient of Zr(N,C) resulting in higher compression stresses after cooling may, to a certain extent, explain why Zr(N,C)-inclusions are found to be less harmful than TiN-inclusions.

Compliance with ethical standards

References

[1] Ishii H, Yagasaki T, Akagi H (2002) Evaluation of giga-cycle fatigue properties of some maraging steels by intermittent ultrasonic fatigue testing. Fatigue Fract Eng Mater Struct 25:831–835

[2] Wang W, Yan W, Duan Q, Shan Y, Zhang Z, Yang K (2010) Study on fatigue property of a new 2.8 GPa grade maraging steel. Mater Sci Eng A 527:3057–3063

[3] Moriyama M, Nagano T, Kawagoishi N, Takaki S, Nagashima E (2001) Effect of shot peening on fatigue strength of 18% Ni maraging steel. JSME Int J Ser A 44(2):301–308

[4] Kawagoishi N, Nagano T, Moriyama M, Kondo E (2009) Improvement of fatigue strength of maraging steel by shot peening. Mater Manuf Process 24:1431–1435

[5] Sun Y, Bell T (1991) Plasma surface engineering of low alloy steel. Mater Sci Eng A 149:419–434

[6] Genel K, Demirkol M, Capa M (2000) Effect of ion nitriding on fatigue behaviour of AISI 4140 steel. Mater Sci Eng A 279:207–216

[7] Hirano T, Shimatani Y, Shiozawa K, Yoshimoto T, Koshi M (2011) Effect of nitriding on very high cycle fatigue

properties of developed high speed steel. Trans J Soc Mech Eng 77(775):427–437

[8] Karliński W, Tacikowski J, Wojtyra K (1999) Fatigue strength of nitrided 18Ni250 and 18Ni300 grade maraging steels. Surf Eng 15(6):483–489

[9] Limodin N, Verreman Y, Tarfa TN (2003) Axial fatigue of a gas-nitrided quenched and tempered AISI 4140 steel: effect of nitriding depth. Fatigue Fract Eng Mater Struct 26:811–820

[10] Wang QY, Kawagoishi N, Li T, Chen Q (2004) Super long life fatigue in nitrided high strength steels. Key Eng Mater 274–276:217–222

[11] Hussain K, Tauqir A, Haq Au, Khan AQ (1999) Influence of gas nitriding on fatigue resistance of maraging steel. Int J Fatigue 21:163–168

[12] Mayer H, Schuller R, Fitzka M, Tran D, Pennings B (2014) Very high cycle fatigue of nitrided 18Ni maraging steel sheet. Int J Fatigue 64:140–146

[13] Schuller R, Fitzka M, Irrasch D, Tran D, Pennings B, Mayer H (2015) VHCF properties of nitrided 18Ni maraging steel thin sheets with different Co and Ti content. Fatigue Fract Eng Mater Struct 38(5):518–527

[14] Naito T, Ueda H, Kikuchui M (1984) Fatigue behavior of carburized steel with internal oxides and nonmartensitic micro-structure near the surface. Metall Trans 15A:1431–1436

[15] Asami K, Sugiyama Y (1985) Fatigue strength of various surface hardened steels. J Heat Treat Technol Assoc 25:147–150

[16] Murakami Y, Takada M, Toriyama T (1998) Super-long life tension-compression fatigue properties of quenched and tempered 0.46% carbon steel. Int J Fatigue 16(9):661–667

[17] Abe T, Furuya Y, Matsuoka S (2004) Gigacycle fatigue properties of 1800 MPa class spring steel. Fatigue Fract Eng Mater Struct 27:159–167

[18] Chai G (2006) The formation of subsurface non-defect fatigue crack origins. Int J Fatigue 28:1533–1539

[19] Akiniwa Y, Stanzl-Tschegg S, Mayer H, Wakita M, Tanaka K (2008) Fatigue strength of spring steel under axial and torsional loading in the very high cycle regime. Int J Fatigue 30:2057–2063

[20] Mayer H, Haydn W, Schuller R, Issler S, Furtner B, Bacher-Höchst M (2009) Very high cycle fatigue properties of bainitic high-carbon-chromium steel. Int J Fatigue 31(2):242–249

[21] Li W, Sakai T, Wakita M, Mimura S (2014) Influence of microstructure and surface defect on very high cycle fatigue properties of clean spring steel. Int J Fatigue 60:48–56

[22] Li SX (2012) Effects of inclusions on very high cycle fatigue properties of high strength steels. Int Mater Rev 57(2):92–114

[23] Zimmermann M (2012) Diversity of damage evolution during cyclic loading at very high numbers of cycles. Int Mater Rev 57(2):73–91

[24] Mayer H (2016) Recent developments in ultrasonic fatigue. Fatigue Fract Eng Mater Struct 39(1):3–29

[25] Sander M, Müller T, Lebahn J (2014) Influence of mean stress and variable amplitude loading on the fatigue behaviour of a high-strength steel in the VHCF regime. Int J Fatigue 62:10–20

[26] Kovacs S, Beck T, Singheiser L (2013) Influence of mean stresses on fatigue life and damage of a turbine blade steel in the VHCF-regime. Int J Fatigue 49:90–99

[27] Murakami Y, Nomotomo T, Ueda T, Murakami Y (2000) On the mechanism of fatigue failure in the superlong life regime ($>10^7$ cycles). Part I: influence of hydrogen trapped by inclusions. Fatigue Fract Eng Mater Struct 23(11):893–902

[28] Murakami Y, Nomotomo T, Ueda T, Murakami Y (2000) On the mechanism of fatigue failure in the superlong life regime ($>10^7$ cycles). Part II: a fractographic investigation. Fatigue Fract Eng Mater Struct 23(11):903–910

[29] Murakami Y, Endo M (1986) Effects of hardness and crack geometries on ΔK_{th} of small cracks emanating from small defects. In: Miller KJ, De Los Rios ER (eds) The behaviour of short fatigue cracks, EGF. Mechanical Engineering Publication, London, pp 27–293

[30] Murakami Y, Endo M (1994) Effects of defects, inclusions and inhomogeneities on fatigue strength. Int J Fatigue 16(3):163–182

[31] Sun C, Lei Z, Xie J, Hong Y (2013) Effects of inclusion size and stress ratio on fatigue strength for high-strength steels with fish-eye mode failure. Int J Fatigue 48:19–27

[32] Furuya Y, Hirukawa H, Kimura T, Hayaishi M (2007) Gigacycle fatigue properties of high-strength steels according to inclusion and ODA sizes. Met Trans A 38A:1722–1730

[33] Spriestersbach D, Grad P, Kerscher E (2014) Influence of different non-metallic inclusion types on the crack initiation in high-strength steels in the VHCF regime. Int J Fatigue 64:114–120

[34] Rohrbach K, Schmidt M (1990) Maraging steels. In: Davis JR, Mills KM, Lampman SR et al (eds) Metals handbook properties and selection: iron, steels, and high-performance alloys, vol 1. ASM International, Materials Park, pp 793–800

[35] Pestov IV, Leonova NK, Maloletnev AY, Perkas MD (1990) Aluminum in maraging steel N18F6M3. Met Sci Heat Treat 32(8):608–612

[36] Rust SW, Rice RC (1992) Statistical distributions. In: Newby JR, Davis JR, Refsnes SK et al (eds) ASM Handbook

Mechanical testing, vol 8. ASM International, Materials Park, pp 628–638

[37] Murakami Y, Nomoto T, Ueda T (1999) Factors influencing the mechanism of superlong fatigue failure in steels. Fatigue Fract Eng Mater Struct 22(7):581–590

[38] Tanaka K, Akiniwa Y (2002) Fatigue crack propagation behaviour derived from S–N data in very high cycle regime. Fatigue Fract Eng Mater Struct 25:775–784

[39] Akiniwa Y, Miyamoto N, Tsuru H, Tanaka K (2006) Notch effect on fatigue strength reduction of bearing steel in the very high cycle regime. Int J Fatigue 28:1555–1565

[40] Murakami Y, Endo M (1992) The area parameter model for small defects and nonmetallic inclusions in fatigue strength: experimental evidences and applications. In: Blom AF, Beevers CJ (eds) Theoretical concepts and numerical analysis of fatigue, Birmingham, UK. Engineering Materials Advisory Services Ltd, Cradley Heath, pp 51–71

[41] Harrison RW, Lee WE (2016) Processing and properties of ZrC, ZrN and ZrCN ceramics: a review. Adv Appl Ceram 115(5):294–307

[42] Ånmark N, Karasev A, Jönsson PG (2015) The effect of different non-metallic inclusions on the machinability of steels. Materials 8:751–783

[43] Brooksbank D, Andrews KW (1972) Stress fields around inclusions and their relation to mechanical properties. J Iron Steel Inst 210:246–255

[44] Davis LC, Allison JE (1993) Residual stresses and their effects on deformation in particle-reinforced metal-matrix composites. Metall Trans A 24A:2487–2496

[45] Yang Q, Lengauer W, Koch T, Scheerer M, Schmid I (2000) Hardness and elastic properties of $Ti(C_xN_{1-x})$, $Zr(C_xN_{1-x})$ and $Hf(C_xN_{1-x})$. J Alloys Compd 309:L5–L9